Synergy of single-atom Ni 1 and Ru 1 sites on CeO 2 for dry reforming of CH 4

Synergy of Single-Atom Ni_1 and Ru_1 Sites on CeO_2 for Dry Reforming of CH_4

Yu Tang,†,‡,⊥ Yuechang Wei,‡,⊥ Ziyun Wang,§,⊥ Shiran Zhang,‡ Yuting Li,‡ Luan Nguyen,‡ Yixiao Li,‡ Yan Zhou,∥ Wenjie Shen,∥ Franklin Feng Tao,*,†,‡ and Peijun Hu*

§ † Institute of Molecular Catalysis and In Situ/Operando Studies, State Key Laboratory of Photocatalysis on Energy and Environment, and College of Chemistry, Fuzhou University, Fuzhou 350116, China
‡ Department of Chemical and Petroleum Engineering, University of Kansas, Lawrence, Kansas 66045, United States
§ School of Chemistry and Chemical Engineering, The Queen's University, Belfast BT9 5AG, U.K.
∥ State Key Lab for Catalysis, Dalian Institute of Chemical Physics, Dalian, 116023, China

Abstract

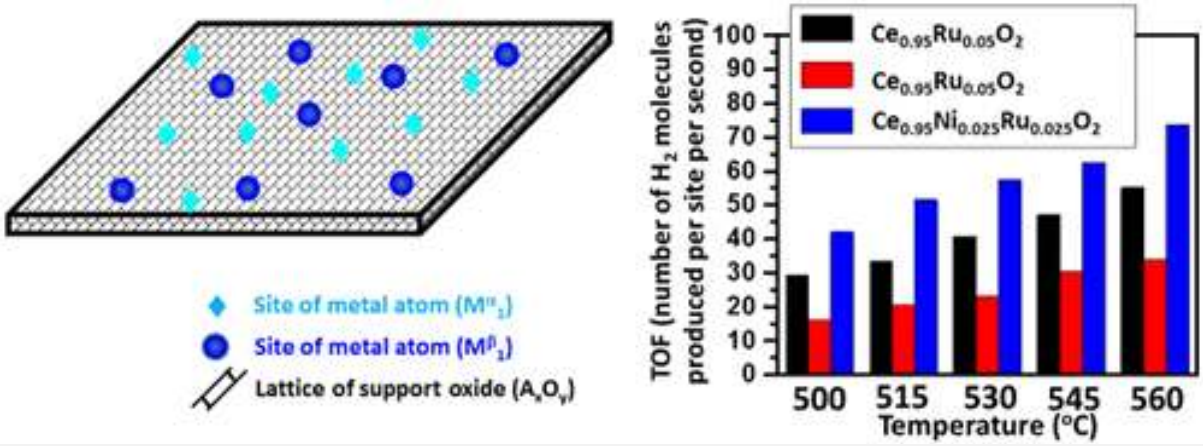

Heterogeneous catalysis performs on specific sites of a catalyst surface even if specific sites of many catalysts during catalysis could not be identified readily. Design of a catalyst by managing catalytic sites on an atomic scale is significant for tuning catalytic performance and offering high activity and selectivity at a relatively low temperature. Here, we report a synergy effect of two sets of single-atom sites (Ni_1 and Ru_1) anchored on the surface of a CeO_2 nanorod, $Ce_{0.95}Ni_{0.025}Ru_{0.025}O_2$. The surface of this catalyst, $Ce_{0.95}Ni_{0.025}Ru_{0.025}O_2$, consists of two sets of single-atom sites which are highly active for reforming CH_4 using CO_2 with a turnover rate of producing 73.6 H_2 molecules on each site per second at 560 °C. Selectivity for producing H_2 at this temperature is 98.5%. The single-atom sites Ni_1 and Ru_1 anchored on the CeO_2 surface of $Ce_{0.95}Ni_{0.025}Ru_{0.025}O_2$ remain singly dispersed and in a cationic state during catalysis up to 600 °C. The two sets of single-atom sites play a synergistic role, evidenced by lower apparent activation barrier and higher turnover rate for production of H_2 and CO on $Ce_{0.95}Ni_{0.025}Ru_{0.025}O_2$ in contrast to

$Ce_{0.95}Ni_{0.05}O_2$ with only Ni_1 single-atom sites and $Ce_{0.95}Ru_{0.05}O_2$ with only Ru_1 single-atom sites. Computational studies suggest a molecular mechanism for the observed synergy effects, which originate at (1) the different roles of Ni_1 and Ru_1 sites in terms of activations of CH_4 to form CO on a Ni_1 site and dissociation of CO_2 to CO on a Ru_1 site, respectively and (2) the sequential role in terms of *first* forming H atoms through activation of CH_4 on a Ni_1 site and *then* coupling of H atoms to form H_2 on a Ru_1 site. These synergistic effects of the two sets of single-atom sites on the same surface demonstrated a new method for designing a catalyst with high activity and selectivity at a relatively low temperature.

1. Introduction

Methane, the major component of natural gas and shale gas, has attracted much attention in the production of chemical intermediates for making liquid fuels and high value chemicals.(1−6) Due to the increase of annual global production of shale gas, chemical industries have started to progressively switch their raw materials from crude oil to shale gas components. Reforming of methane with CO_2 or H_2O has been one of the most important processes since it produces syngas, one of the most important intermediates for producing liquid fuels and synthesizing high-value chemicals through established industrial processes.(1,5−7)

The current industrial process of reforming methane on supported Ni metal nanoparticle catalysts undergoes at a temperature higher than 800 °C.(8−10) Unfortunately, it faces two challenges. First, the catalyst is readily deactivated due to sintering of these supported metallic Ni nanoparticles at high temperature in an environment of reducing gases (CO + H_2).(11) The sintering significantly decreases dispersion of Ni atoms of a supported Ni catalyst; therefore, the number of exposed Ni atoms of the catalyst decreases dramatically. Second, a side reaction of methane pyrolysis is readily performed on the surface of metallic Ni nanoparticles.(12,13) Due to the very high binding energy of C atoms of CH_n (n = 0–3) species on Ni atoms of metallic Ni nanoparticles, metallic Ni nanoparticles are very active for breaking the C–H bond of methane. The rapid catalytic pyrolysis produces layers of carbon atoms on the surface of a Ni catalyst, which is known as coke.(14,15) The formation of coke completely blocks methane from accessing Ni atoms of the catalyst, making the catalyst completely poisoned. In addition, the quite high catalytic temperature of supported Ni nanoparticles (800 °C or higher) requires a significant amount of energy. Facing these challenges, it would be ideal if methane reforming could be done at a relative low temperature without coke formation; for this purpose, significant efforts have been made by the groups of Rodriguez and others.(16−18)

To avoid the formation of coke on the surface of Ni catalysts, we proposed to design a catalyst which can activate CH_n (n = 0–3) and their intermediates.

Based on our recent studies that showed that binding energy of a methane molecule on a metal atom at a cationic state is typically lower than that on a metal atom at a metallic state,(19−23) here we propose to anchor Ni atoms of a cationic state instead of Ni atoms of a metallic state to activate methane or CO_2 molecules, avoiding strong binding to CH_n (n = 0–3) species. In addition, to spatially limit any potential coupling between carbon atoms or CH_n (n = 0–3) species adsorbed on continuously packed Ni atoms to form precursor of a coke layer, Ni atoms are spatially anchored on the surface in the format of single-atom sites as shown with bright blue diamonds (Ni atoms) in Figure 1.

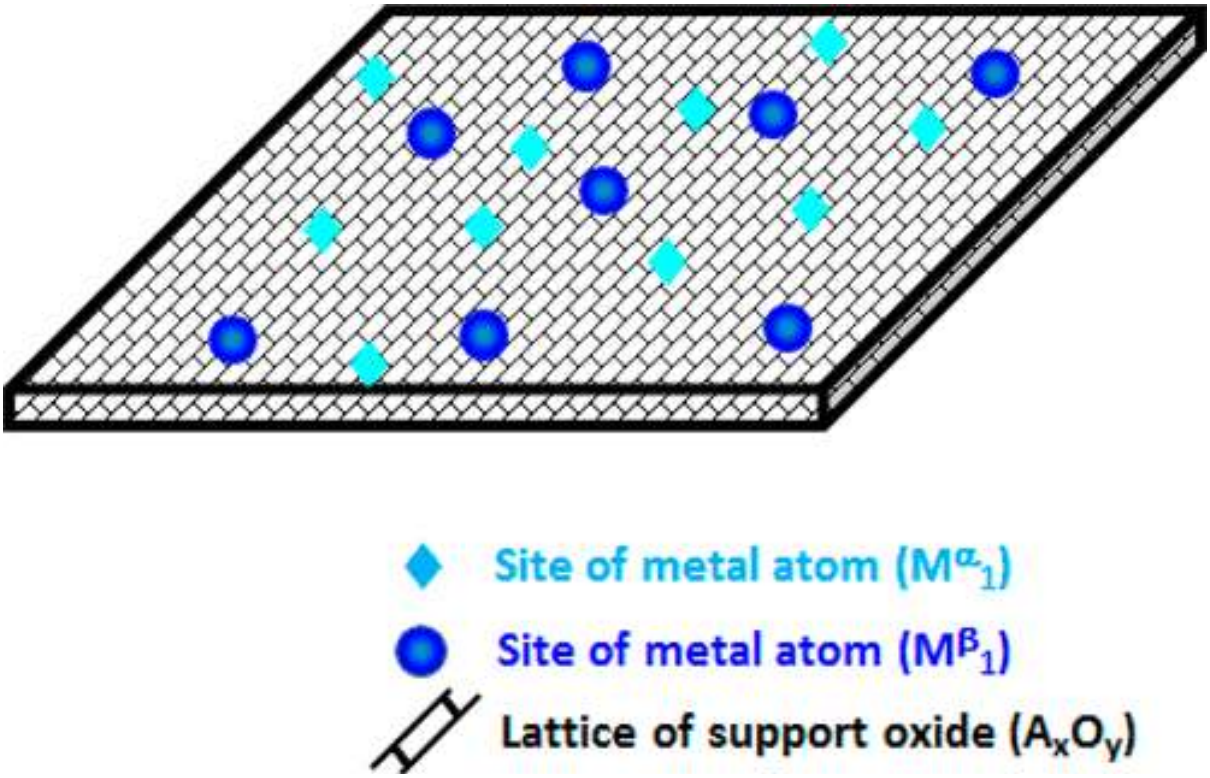

Figure 1. Schematic of a catalyst surface consists of two sets of single-atom sites including single-atom M^{α} sites (green diamonds) and single-atom M^{β} sites (blue balls) anchored on the surface lattice of support (black mesh). This schematic represents the surface structure of $Ce_{0.95}Ni_{0.025}Ru_{0.025}O_2$ on which Ni_1 and Ru_1 cations are single-atom sites; CeO_2 is the support; both Ni_1 and Ru_1 are singly dispersed on CeO_2.

Ru is active in activating CO_2 by dissociation of C–O of CO_2 to CO(1,8,9,18,20,24−26) Thus, it is chosen as the guest metal atom to activate CO_2. The surface of CeO_2 has a high density of oxygen vacancies.(17,27,28) It is expected that oxygen vacancies of the CeO_2 surface could participate into the activation of CO_2. In addition, the high affinity of surface lattice oxygen atoms to metal atoms could stabilize these guest cations and keep them singly dispersed. Thus, CeO_2 was chosen as a support to anchor the two sets of single atoms, Ni_1 and Ru_1.

Catalysts consisting of CeO_2 nanorods and two sets of single-atom sites, Ni_1 or/and Ru_1, were successfully synthesized in this work. Operando studies of chemical and coordination environments during catalysis revealed that both Ni and Ru cations are singly dispersed and remained at the cationic state during catalysis. This catalyst is highly active for reforming methane with CO_2. Selectivity for producing H_2 reaches 98.5% at 600 °C. Synergy effects between single-atom sites Ni_1 and Ru_1 at low concentration of 2.5% Ni and 2.5% Ru were proved. Computational studies proposed a molecular mechanism for the synergistic effects of Ni_1 and Ru_1 sites in reforming CH_4 with CO_2. This work suggests an avenue in designing new catalysts with high activity and selectivity at a relatively low temperature.

2. Experimental and Computational Methods

The CeO_2-based nanorods were synthesized with a modified hydrothermal method.(29−31)Typically, 4 mmol of metal nitrite precursors was dissolved in 10 mL of deionized water and then added to 70 mL of NaOH solution (6 mol/L) dropwise under vigorous stirring. A precipitate was formed during stirring. After being stirred for 30 min at room temperature, the slurry was transferred to a stainless-steel autoclave (100 mL) with PTFE lining and maintained at 120 °C for 24 h. Then the autoclave was cooled to room temperature naturally. The solid in the autoclave was separated by centrifugation and then washed with water until the pH was about 7.0. The solid separated upon the centrifugation was collected and then dried in an oven at 80 °C for 12 h. After the drying step, the product was ground into fine powder and then calcined at 400 °C for 2 h in air. Catalytic performances of a catalyst were measured with a fixed-bed flow reactor. Specific catalytic conditions can be found in section 1 of the Supporting Information.

The high-resolution transmission electron microscope (HR-TEM) images and high angle annular dark field (HAADF) images in the STEM mode of used catalysts were taken by using a FEI Tecnai F20 XT. Powder X-ray diffraction (XRD) patterns of used catalysts were recorded with a Rigaku Ultimate IV operating in reflection mode with Cu Kα radiation that was monochromated with a secondary graphite monochromator. Extended X-ray absorption fine structure spectra (EXAFS) at the Ru K-edge and Ni K-edge of catalysts during catalysis were collected at a beamline 2-2 at SSRL and ISS end station (8-ID) at NSLS-II. Details of characterization can be found in section 2 of the Supporting Information.

Ambient-pressure X-ray photoelectron spectroscopy is an analytical method by which surface of a material in gas phase at certain pressure (mostly subtorr or a couple of torr of gas) is examined when gas is remained during data acquisition. The upper limit of gas pressure is limited to the brightness of the X-ray beam and other factors. The surface chemistry of a catalyst uncovered under this condition can be correlated with catalytic performance of the catalyst. The Ce 3d, Ni 2p, Ru 3p, and O 1s of a catalyst before catalysis were

collected at 150 °C for increasing conductivity of CeO_2-based samples and thus minimizing surface charging. For in situ/operando studies of surface of the catalyst during catalysis at a temperature higher than 150 °C, there is no charging effect.
All the DFT calculations were carried out with a periodic slab model using the Vienna *ab initio* simulation program (VASP).(32−35) The generalized gradient approximation (GGA) was used with the Perdew–Burke–Ernzerhof (PBE)(36) exchange-correlation functional. The projector-augmented wave (PAW) method(37,38) was utilized to describe the electron–ion interactions; the cutoff energy for the plane-wave basis set was 450 eV. Details of DFT calculations can be found in section 3 of the Supporting Information.

3. Results and Discussion

3.1. Preparation of CeO_2 Nanorods with anchored Ni_1 and Ru_1 Sites or Coanchored Ni_1 and Ru_1 Sites

Three type of catalysts, namely Ru_1/CeO_2, Ni_1/CeO_2, and $Ru_1 + Ni_1/CeO_2$, were prepared with the specific protocol described in the Experimental Section. The loading concentrations of Ru, Ni, and the total of Ru and Ni in the three catalysts are 5.0 wt % for $Ce_{0.95}Ru_{0.05}O_2$, 5.0 wt % for $Ce_{0.95}Ni_{0.05}O_2$, and 2.5 wt % + 2.5 wt % for $Ce_{0.95}Ni_{0.025}Ru_{0.025}O_2$, respectively. Morphology and lattice fringes of the used Ru_1/CeO_2, Ni_1/CeO_2, and Ru_1+Ni_1/CeO_2 were examined with HRTEM. The observed diffraction peaks of $Ru_1 + Ni_1/CeO_2$ catalyst in the XRD pattern in Figure S1 in the Supporting Information were indexed to (111), (200), (220), and (311) planes, which correspond to a typical fluorite structure of CeO_2 (JCPDS 43-1002).(29) No characteristic diffraction peaks belonging to NiO and RuO_2 nanoparticles could be detected, suggesting the lack of NiO and RuO_2 nanoparticles. Thus, these used catalysts, Ru_1/CeO_2, Ni_1/CeO_2, and $Ru_1 + Ni_1/CeO_2$, remain the fluorite phase of pure CeO_2 without formation of NiO or RuO_2 nanoparticles on them. XRD patterns of the used catalysts suggest that these catalysts have high structural stability during catalysis at 600 °C.
High-resolution TEM images of the used catalyst $Ru_1 + Ni_1/CeO_2$ allow for identification of lattice fringes (Figures 2 and 3). The dominantly exposed planes of $Ce_{0.95}Ru_{0.05}O_2$, $Ce_{0.95}Ni_{0.05}O_2$, and $Ce_{0.95}Ru_{0.025}Ni_{0.025}O_2$ catalysts exhibit interplanar spacing of 2.80 Å, which corresponds to (200) planes of CeO_2.(29) As Ni and Ru atoms have lower atomic number than a Ce atom, it is challenging to distinguish Ni or Ru atoms from Ce atoms of CeO_2 nanorods by the HAADF–STEM technique. Many efforts were made in checking whether NiO or/and RuO_2 could have been formed on the surface of CeO_2 nanorods. No NiO or RuO_2 nanoparticles were observed on the surfaces of CeO_2 nanorods of these catalysts even at different tilting angles of specimens in HAADF–STEM. These structural characterizations of catalysts used for reforming CH_4 with CO_2 suggest that Ru and Ni cations are highly dispersed. In fact, they are singly dispersed; their single dispersions in terms

of single-atom sites of Ni_1 and Ru_1 of these used catalysts were confirmed with operando EXAFS studies to be presented in next sections.

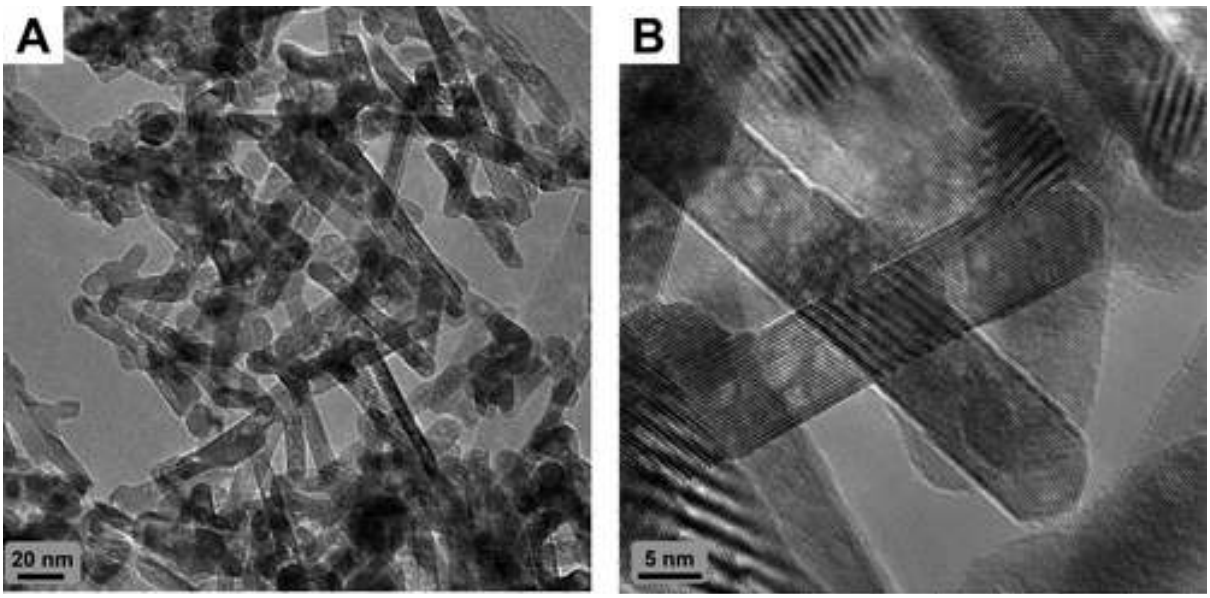

Figure 2. HRTEM images of $Ce_{0.95}Ni_{0.025}Ru_{0.025}O_2$ catalyst after it was used for reforming of methane with CO_2 at 600 °C performed in a fixed-bed flow reactor.

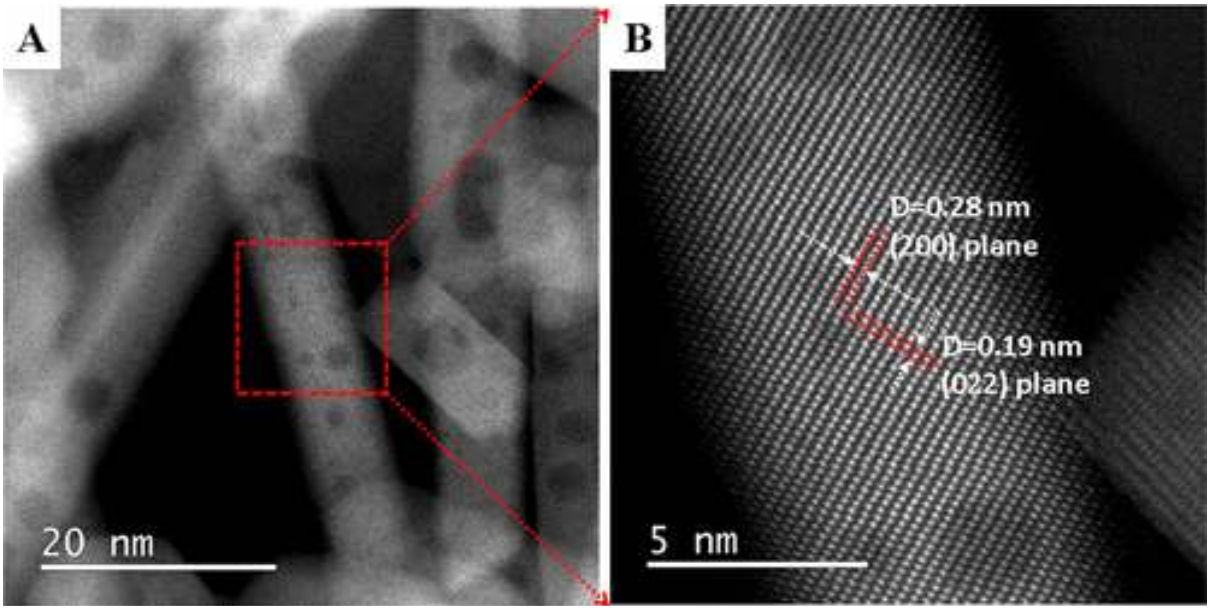

Figure 3. Aberration-corrected STEM images of $Ce_{0.95}Ni_{0.025}Ru_{0.025}O_2$ catalyst after it was used for reforming of CH_4 with CO_2 at 600 °C performed in a fixed-bed flow reactor.

Figure 3 presents the aberration-corrected HAADF–STEM images of a $Ce_{0.95}Ni_{0.025}Ru_{0.025}O_2$ catalyst which was used for reforming CH_4 at 600 °C. The used $Ce_{0.95}Ni_{0.025}Ru_{0.025}O_2$ catalyst retains the original morphology of nanorods after catalysis at 600 °C (Figure 3a). The two-dimensional lattice fringe of the used $Ce_{0.95}Ni_{0.025}Ru_{0.025}O_2$ can be readily identified in Figure 3b. The interplanar distances of the CeO_2 nanorods of the used catalyst $Ce_{0.95}Ni_{0.025}Ru_{0.025}O_2$ along the two directions marked with red dashed lines in Figure 3b are 2.8 and 1.9 Å, which correspond to the interplanar distance of two adjacent planes of (200) and that of two adjacent (220) planes of CeO_2, respectively. The identification of these lattice fringes shows that (110) is one of the preferentially formed plane prependicualr to (200) and (022), consistent with that reported in literatures.(29,31) No NiO and RuO_2 nanoparticles were observed from the used catalyst $Ce_{0.95}Ni_{0.025}Ru_{0.025}O_2$ (Figure 3). Similar to $Ce_{0.95}Ni_{0.025}Ru_{0.025}O_2$, (110) planes of $Ce_{0.95}Ni_{0.05}O_2$ and $Ce_{0.95}Ni_{0.05}O_2$ are the preferentially exposed surfaces, and there is lack of NiO or RuO_2 nanoparticles formed on the surface of nanorods of the two used catalysts.

3.2. Catalytic Performance of Single-Atom Ru_1 and/or Ni_1 Sites on Ceria Support

Catalytic performances of three $Ce_{1-x-y}Ni_xRu_yO_2$ catalysts ($Ce_{0.95}Ni_{0.05}O_2$ and $Ce_{0.95}Ru_{0.05}O_2$, $Ce_{0.95}Ni_{0.025}Ru_{0.025}O_2$) for reforming methane with CO_2 in terms of conversion of CH_4 and selectivity for production of H_2 and ratio of H_2 to CO were studied with a fixed-bed flow reactor in the temperature range of 300–600 °C. For the measurements of catalytic performances, 50 mg of each of the three catalysts diluted with 300 mg of purified quartz was loaded to the reactor. A 40 mL/min mixture of CH_4 (1% in Ar) and CO_2 (1% in Ar) was mixed and flown through the catalyst bed. Selectivities for producing H_2 on $Ce_{0.95}Ni_{0.05}O_2$ and $Ce_{0.95}Ru_{0.05}O_2$ at 600 °C are 80.0% and 82.9%, respectively (black and red lines in Figure 4b). Compared to $Ce_{0.95}Ni_{0.05}O_2$ and $Ce_{0.95}Ru_{0.05}O_2$, $Ce_{0.95}Ni_{0.025}Ru_{0.025}O_2$ exhibits a higher selectivity of 98.5% for producing H_2 at 600 °C (blue line in Figure 4b). As shown in Figure 4a, the conversion of CH_4 on 50 mg $Ce_{0.95}Ni_{0.025}Ru_{0.025}O_2$, 91% is obviously higher than half of the total of conversions of 50 mg $Ce_{0.95}Ru_{0.05}O_2$ (83%) and 50 mg of $Ce_{0.95}Ni_{0.05}O_2$ (63%) at 600 °C (Figure 4a), 73% $\left(=\frac{83\%+63\%}{2}\right)$, which suggests a synergy effect of Ni and Ru cations on reforming CH_4 with CO_2. In addition, the yield of H_2 at 600 °C (90%) is much higher than half of total yield of $Ce_{0.95}Ni_{0.05}O_2$ (65%) and $Ce_{0.95}Ru_{0.05}O_2$ (52%), 58.5% $\left(=\frac{65\%+50\%}{2}\right)$. Here, we assume that the number of sites (Ni_1 or Ru_1) on topmost layer of CeO_2 is proportional to the nominal composition of the three catalysts and that the numbers of Ni_1 and Ru_1 sties of $Ce_{0.95}Ni_{0.025}Ru_{0.025}O_2$ are half of the number of Ni_1 sites of $Ce_{0.95}Ni_{0.05}O_2$ and half of the number of Ru_1 sites of $Ce_{0.95}Ni_{0.05}O_2$, respectively.

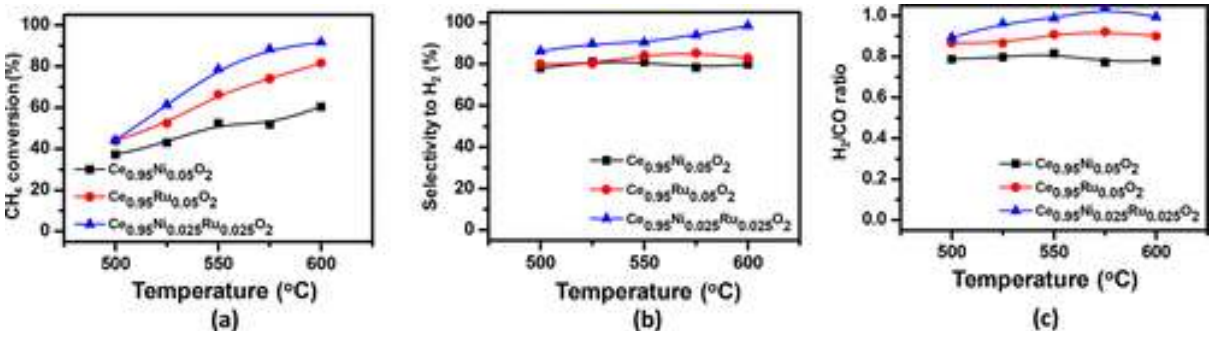

Figure 4. Catalytic performances of $Ce_{0.95}Ni_{0.05}O_2$, $Ce_{0.95}Ru_{0.05}O_2$, and $Ce_{0.95}Ni_{0.025}Ru_{0.025}O_2$ for reforming of CH_4 with CO_2. (a) Conversion of CH_4, (b) selectivity for producing H_2, and (c) H_2/CO ratio. $Ce_{1-x-y}Ni_xRu_yO_2$ (50 mg) diluted with 300 mg purified quartz was loaded to the fixed-bed flow reactor. CH_4 (20 mL/min) (1.0%) and 20 mL/min CO_2 (1.0%) were mixed and then flown into the reactor.

To explore whether the observed synergistic effect is an intrinsic characteristic or just a matter of number of sites of these catalysts, kinetic studies of $Ce_{0.95}Ni_{0.05}O_2$ and $Ce_{0.95}Ru_{0.05}O_2$ and $Ce_{0.95}Ni_{0.025}Ru_{0.025}O_2$ were performed under the same conditions. In these kinetic studies, a certain amount of catalyst diluted with 300 mg of purified quartz was loaded to a fixed-bed flow reactor, and a mixture of 40 mL/min 1.0% CH_4 and 40 mL/min 1.0% CO_2 was introduced to the reactor. Catalytic performances on these catalysts were measured in the whole temperature range of kinetics studies, 500–560 °C. Figure 5 presents Arrhenius plots of $Ce_{0.95}Ni_{0.05}O_2$, $Ce_{0.95}Ru_{0.05}O_2$, and $Ce_{0.95}Ni_{0.025}Ru_{0.025}O_2$ in the temperature range of 500–560 °C. All conversions in this temperature range are definitely lower than 20%. The *Y* axis of Figure 5 is the natural log of the production rate of H_2 or CO (number of molecules produced per site per second). Apparent activation barriers were calculated through the slopes of these plots in Figure 5. Notably, on the basis of the production of H_2, the measured activation barrier of $Ce_{0.95}Ni_{0.025}Ru_{0.025}O_2$ (51.7 kJ/mol) is obviously lower than those of $Ce_{0.95}Ni_{0.05}O_2$ (66.0 kJ/mol) and $Ce_{0.95}Ru_{0.05}O_2$ (75.6 kJ/mol). On the basis of the production of CO, the measured activation barrier of $Ce_{0.95}Ni_{0.025}Ru_{0.025}O_2$ (41.5 kJ/mol) is also obviously lower than those of $Ce_{0.95}Ni_{0.05}O_2$ (61.2 kJ/mol) and $Ce_{0.95}Ru_{0.05}O_2$ (71.3 kJ/mol). This intrinsic difference in dry reforming between $Ce_{0.95}Ni_{0.05}O_2$ (or $Ce_{0.95}Ru_{0.05}O_2$) and $Ce_{0.95}Ni_{0.025}Ru_{0.025}O_2$ confirmed the synergistic effect between anchored Ni and Ru cations; this synergistic effect of Ni_1 and Ru_1 sites on $Ce_{0.95}Ni_{0.025}Ru_{0.025}O_2$ decreases the activation barriers for reforming methane with CO_2.

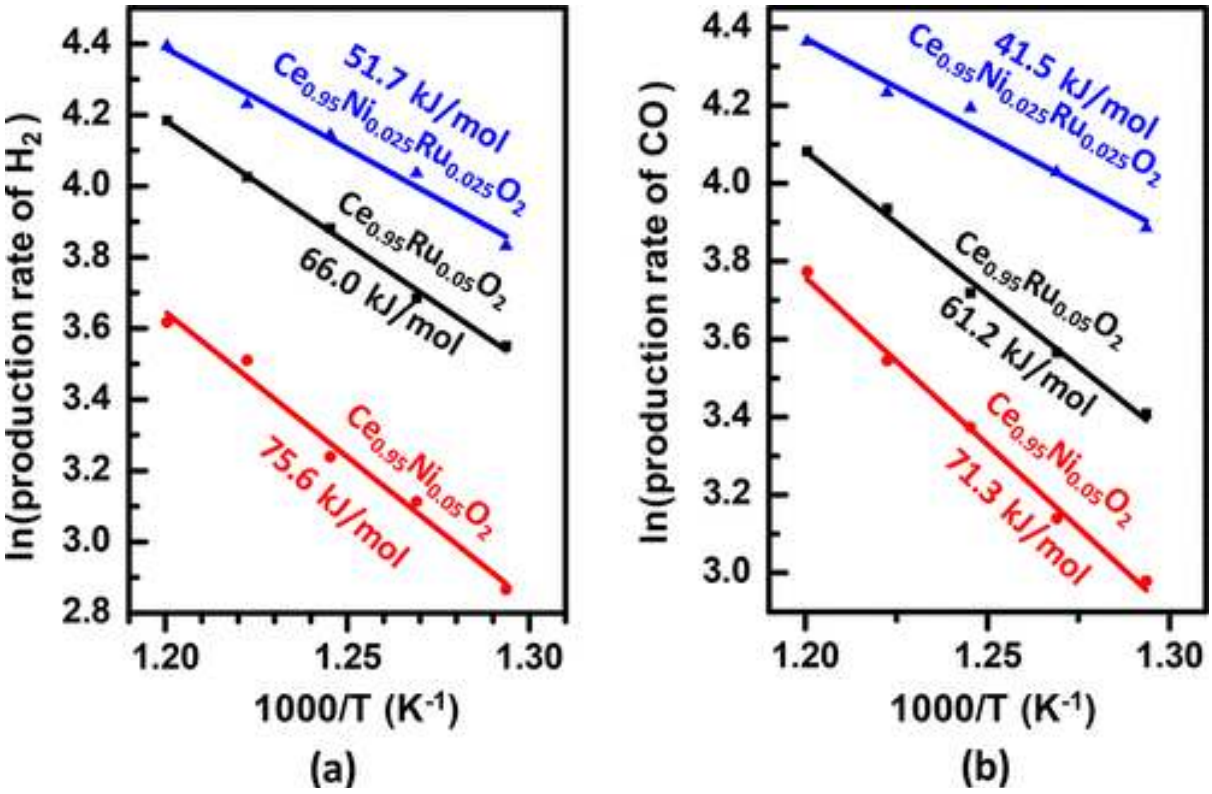

Figure 5. Arrhenius plot in terms of the rate of product of (a) H_2 and (b) CO catalyzed by the $Ce_{1-x-y}Ni_xRu_yO_2$ catalysts. Blue: 5 mg of $Ce_{0.95}Ni_{0.025}Ru_{0.025}O_2$ diluted with 300 mg of purified quartz. Black: 15 mg of $Ce_{0.95}Ru_{0.05}O_2$diluted with 300 mg of purified quartz. Red: 20 mg of $Ce_{0.95}Ni_{0.05}O_2$ diluted with 300 mg of purified quartz. Mixture of 40 mL/min of 1.0% CH_4 and 40 mL/min of 1.0% CO_2 was introduced during kinetic studies. *Y*-axis is the natural log of the production rate of H_2(*a*) or CO (b) in a unit: the number of H_2(or CO) molecules formed on a metal site per second. For $Ce_{0.95}Ni_{0.025}Ru_{0.025}O_2$, both Ni and Ru atoms of the topmost layer were counted as active sites in the calculation of production rate (the number of H_2 or CO molecules produced on a site per second). For $Ce_{0.95}Ru_{0.05}O_2$ and $Ce_{0.95}Ni_{0.05}O_2$, only Ni or Ru cations of the topmost layer were considered as active sites. The numbers of Ni_1 atoms of $Ce_{0.95}Ni_{0.05}O_2$, Ru_1 atoms of $Ce_{0.95}Ru_{0.05}O_2$, or both Ni_1 and Ru_1 of $Ce_{0.95}Ni_{0.025}Ru_{0.025}O_2$ were measured with AP-XPS during catalysis.

As shown in Figure 5, the measured apparent activation barrier for producing CO is different from that for producing H_2 on the same catalyst. It is known that for many reactions more than one step could have activation barriers close to the step of the highest activation barrier; in fact, these steps of a catalytic cycle can be considered as rate-determining steps as well. In other words, to some extent there could be more than one rate-determining step in a complete catalytic cycle. However, how these rate-determining steps collectively give a measurable apparent activation barrier is still a debatable topic in the field of computational and experimental studies. Here, the measured difference between apparent activation barriers for producing CO

and that for producing H_2 suggests that some of the rate-determining steps for producing CO are different from those of the rate-determining steps for producing H_2. In fact, *both* the complexity of rate-determining steps for CO and H_2*and* the unknown correlation between barriers of rate-determining steps and observable apparent activation barrier could result in the difference between the measured apparent activation barrier for producing CO and that for producing H_2.

As shown in Figure 4c, the ratio of H_2/CO increases as a function of catalysis temperature, which is consistent with the evolution of equilibrium H_2/CO ratio in reforming of CH_4 with CO_2 as a function of temperature calculated with ASPEN; in this calculation the equilibrium H_2/CO ratios at different temperatures were calculated when H_2O was considered as a product formed from reverse water–gas shift (RWGS) of CO_2 and H_2. In these ASPEN calculations, we built a fixed-bed flow reactor, input the initial concentrations of CH_4, (0.5%) and CO_2 (0.5%), and took CO, H_2, and H_2O as products. Figure S5 plots the calculated conversion of CH_4 as a function of temperatures at 300–600 °C. At 600 °C, the conversion of CH_4 is 97%. In addition, the calculated ratios of H_2/CO were plotted in Figure S6; they increase as a function of catalysis temperature. This temperature evolution of H_2/CO ratio calculated with ASPEN while H_2O was a byproduct and RWGS as a side reaction (Figure S6) is in agreement with the one measured (Figure 4c). This consistency suggests that RWGS is definitely a side reaction of dry reforming of CH_4.

Turnover frequencies (TOFs) of reforming of methane with CO_2 over these catalysts were calculated with yields of H_2 and CO measured under a kinetics-controlled regime. For catalysts $Ce_{0.95}Ni_{0.05}O_2$ or $Ce_{0.95}Ru_{0.05}O_2$, the number of Ni_1 or Ru_1 atoms on the topmost layer of the catalyst was, respectively, used as a denominator in the calculation of TOF. In the case of $Ce_{0.95}Ni_{0.025}Ru_{0.025}O_2$, the total number of both Ni_1 and Ru_1 atoms on the topmost layer of this catalyst was counted as an active site of reforming CH_4 in the calculations of TOFs. The calculations of numbers of Ni_1 or/and Ru_1 sites on these catalysts and the corresponding TOFs can be found in section 2 of the Supporting Information. As shown in Figure 6, TOF of $Ce_{0.95}Ni_{0.025}Ru_{0.025}O_2$ is definitely higher than that of $Ce_{0.95}Ni_{0.05}O_2$ and $Ce_{0.95}Ru_{0.05}O_2$ at the same temperature in the temperature range 500–560 °C, further confirming the synergy effect between Ru_1 and Ni_1 sites on CeO_2 in reforming of CH_4 with CO_2.

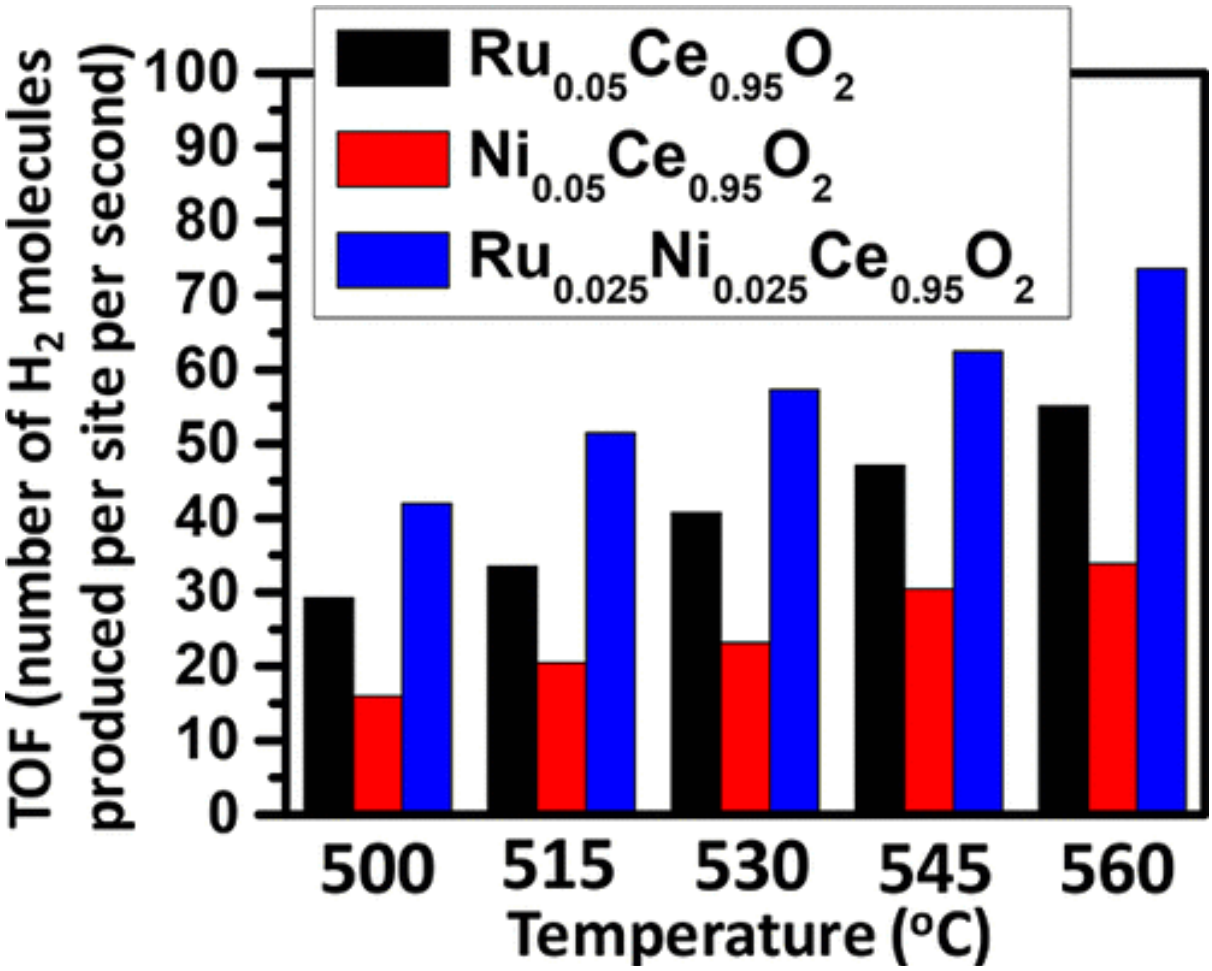

Figure 6. Turnover frequency (TOF) of reforming CH_4 with CO_2 in terms of hydrogen production per Ni_1 site of $Ce_{0.95}Ni_{0.05}O_2$, per Ru_1 site of $Ce_{0.95}$ $Ru_{0.05}O_2$, and per $_1$ or Ru_1 site for $Ce_{0.95}Ni_{0.025}Ru_{0.025}O_2$ at 500–560 °C. In the calculation of TOFs, the number of catalytic sites for $Ce_{0.95}Ni_{0.025}Ru_{0.025}O_2$ is the total number of Ni and Ru atoms of the topmost surface layer of $Ce_{0.95}Ni_{0.025}Ru_{0.025}O_2$. The number of Ni atoms on the topmost layer of $Ce_{0.95}Ni_{0.05}O_2$, the numbers of Ru_1 atoms on the topmost layer of $Ce_{0.95}Ru_{0.05}O_2$, and the total number of Ni_1 and Ru_1 atoms on the topmost layer of $Ce_{0.95}Ni_{0.025}Ni_{0.025}O_2$ were measured with an ambient-pressure X-ray photoelectron spectrometer during catalysis under kinetics control regime.

The distance between Ni_1 and Ru_1 cations of $Ce_{1-x-y}Ni_xRu_yO_2$ is expected to be a factor influencing catalytic performance. To address how a relative distance between Ni_1 and Ru_1 on CeO_2 could influence a catalytic performance, a much larger variation in concentration of Ni_1 (or Ru_1) on surfaces of $Ce_{1-x-y}Ni_xRu_yO_2$ is necessary. To largely decrease the relative distance, one has to increase the loadings of Ni and Ru largely. Unfortunately, Ni (or Ru) at high loadings can readily form metal or oxide nanoparticles, which could readily prevent us from studying the synergistic effect between two sets of single atom sites. To largely increase the average distance between Ni_1 and Ru_1 sites, one has to largely decrease the loadings of these metal atoms. However, it is quite

challenging to characterize chemical and coordination environments of these single-atom sites if the loading of Ni or Ru is too low. Facing these challenges, how the average distance between Ni_1 and Ru_1 could influence the synergetic effect was not explored here.

3.3. Operando Studies of Catalyst during Catalysis

Surface chemistry of catalysts during catalysis was investigated by AP-XPS. On the basis of the literature,(39,40) one of the photoemission features of Ce^{3+} is at 885.2 eV which does not overlap with photoemission features of Ce^{4+} of CeO_2.(39,40) As shown in Figure 7a1, there is nearly lack of the photoemission feature of Ce^{3+} at 885.2 eV. It suggests that the fraction of Ce^{3+} in the surface region of $Ce_{0.95}Ni_{0.025}Ru_{0.025}O_2$ before catalysis is quite low, forming a valley in the region of 885.2 ± 1.5 eV. Compared to the catalyst before catalysis, the fraction of Ce^{3+} during catalysis at 550 °C is obviously higher than that before catalysis, as evidenced by the formation of a plateau in the region of 885.2 ± 1.5 eV during catalysis at 550 °C (Figure 7a2) instead of a valley-like feature (Figure 7a1). The deconvolution of Ce 3d collected at 550 °C during catalysis suggests that the $Ce^{3+}/(Ce^{3+} + Ce^{4+})$ is 20.3%, which is much higher than the 2.3% of catalyst at 150 °C in UHV. In terms of the O*1s* feature before catalysis, the major oxygen species represented by the O*1s* feature is surface lattice oxygen. A component at 532.0 eV in the O 1s spectrum of the fresh catalyst (Figure 7b1) was observed and assigned to −OH groups formed on the surface of ceria.(39,41) It is formed through dissociative chemisorption of water molecules on oxygen vacancies in the cooling process in air upon calcination at a high temperature during catalyst preparation. The atomic fraction of these species of hydroxyl groups decreased along the increase of catalysis temperature. Because Ru 3d overlaps with C 1s, Ru 3p spectra were collected here to analyze Ru. As shown in the Figure 7c1, Ru is at an oxidizing state in the fresh catalyst of $Ce_{0.95}Ni_{0.025}Ru_{0.025}O_2$. When $Ce_{0.95}Ni_{0.025}Ru_{0.025}O_2$ was under catalysis conditions at a specific temperature (Figure 7c2), binding energies of Ru 3p downshifted to the side of lower binding energy. This downshift of binding energy of Ru 3p indicates an increase of electron density of Ru atoms. This is due to a partial reduction of Ru atoms or a change of chemical or/and coordination environment of Ru atoms to an environment of Ru with a higher electron density. Notably, the binding energy (462.4 eV) of Ru 3p of Ru atoms during catalysis at 550 °C (Figure 7c2) is still higher than the metallic Ru 3p, which is 461.7 eV;(42) it suggests that Ru atoms of $Ce_{0.95}Ni_{0.025}Ru_{0.025}O_2$ are at a cationic state.

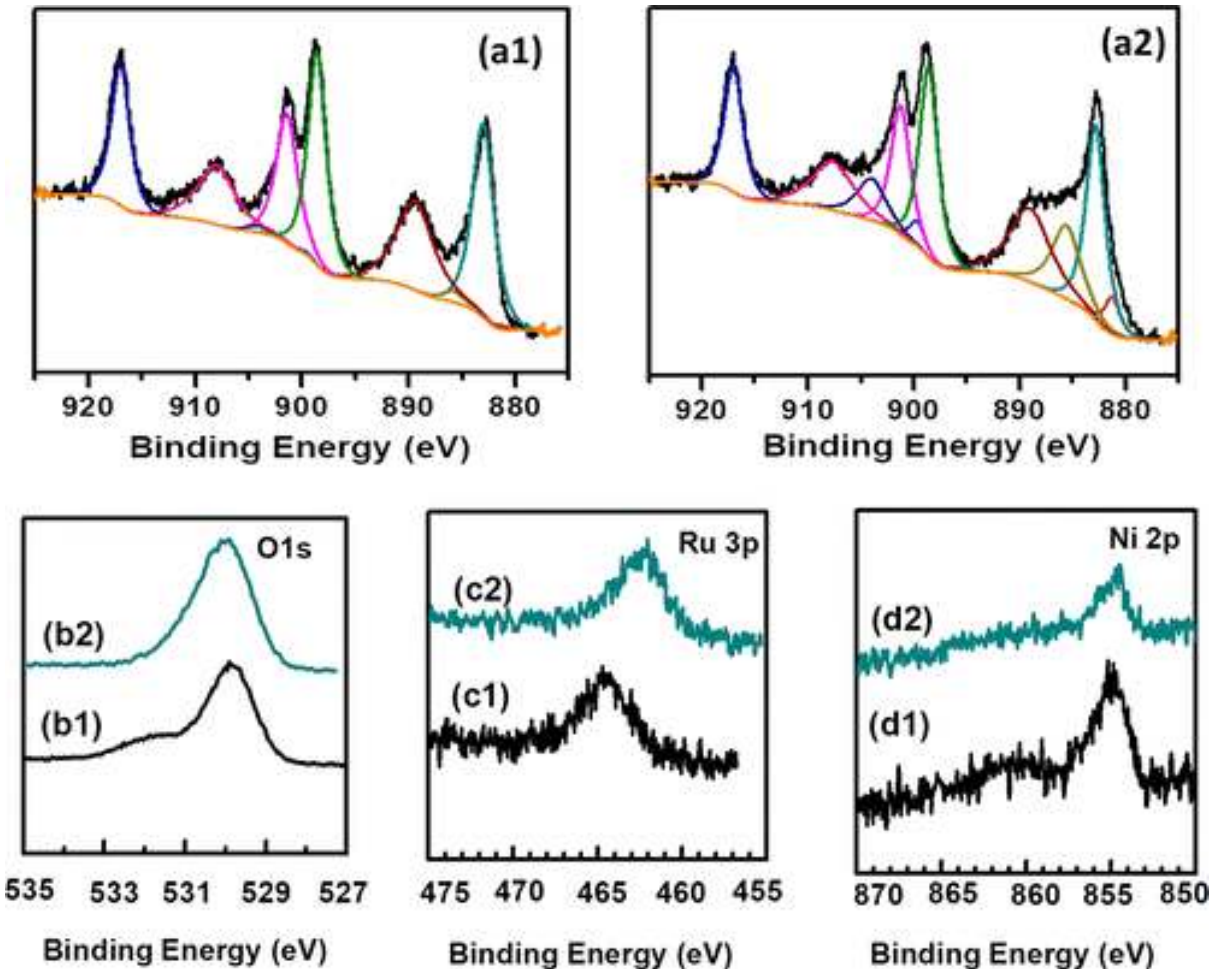

Figure 7. Ce 3d, O 1s, Ru 3p, and Ni 2p photoemission features from AP-XPS studies of $Ce_{0.95}Ni_{0.025}Ru_{0.025}O_2$ during reforming of CH_4 with CO_2. (a1, b1, c1, and d1) Photoemission feature before catalysis, (a2, b2, c2, and d2) photoemission feature during catalysis at 550 °C. The molar fractions of CO_2 and CH_4 in the flowing mixture are 50% and 50%.

Figure 7d presents the Ni 2p3/2 of $Ce_{0.95}Ni_{0.025}Ru_{0.025}O_2$ collected under different conditions. The photoemission feature of Ni 2p1/2 was not shown in this figure so that the photoemission feature of Ni 2p3/2 can be presented clearly. Although a slight down shift of Ni 2p 3/2 was observed during catalysis (Figure 7d2) compared to that before catalysis (Figure 7d1), Ni atoms of this catalyst during catalysis with Ni 2p3/2 at 854.8 eV remained at an oxidative state based on the binding energy of Ni 2p photoelectrons of NiO at 853.8 eV.(43) In the case of NiO nanoparticles, a very strong satellite peak of Ni 2p 3/2 was clearly observed at 861.4 eV;(43) this satellite peak is originated at long-range scattering of structure of ···Ni–O–Ni–O–Ni–O··· in the lattice of a NiO nanoparticle whose surface region has interdigitated Ni and O atoms.(24,44,45) By checking this satellite peak, we can judge whether there is a Ni–O–Ni structure or not on the surface region of the catalyst. For instance, Ni 2p3/2 of singly dispersed Ni atoms in micropore of ZSM-5(18) and on the surface of $Co_{2.25}Ni_{0.75}O_4$ nanoparticles does not exhibit such a satellite

peak in our previous studies.(24) Here, the lack of satellite peak next to the Ni 2p3/2 main peak (Figure 7d2) suggests that Ni atoms during catalysis at 550 °C are singly dispersed instead of formation of NiO lattice, ···Ni–O–Ni–O–Ni-O···. Thus, the AP-XPS studies of $Ce_{0.95}Ni_{0.025}Ru_{0.025}O_2$ clearly suggest that Ni and Ru atoms in this catalyst during catalysis are at a cationic state instead of a metallic state.(46) This was confirmed by inoperando studies of chemical and coordination environments of Ni and Ru atoms during catalysis with EXAFS (Figure 8).

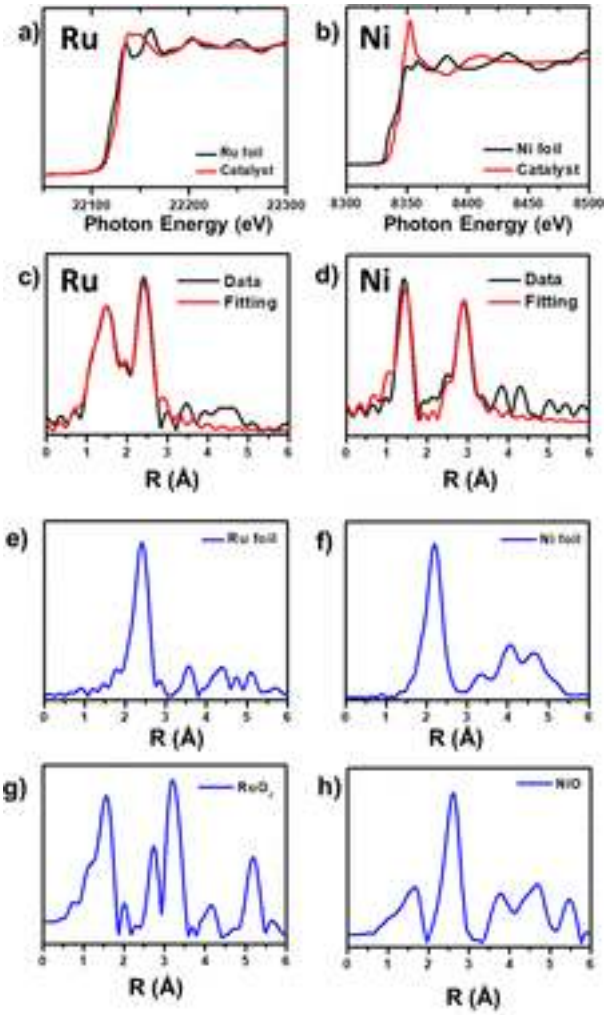

	CN	Distance (Å)	ss
Ru-O	2.08±0.65	1.86±0.06	0.00200
Ru-O	2.41±0.63	2.11±0.05	0.00200
Ru-Ce	2.73±0.40	2.78±0.02	0.00200
Ni-O	3.38±0.35	1.90±0.02	0.00456
Ni-Ce	2.80±0.85	3.10±0.07	0.00828

i)

Figure 8. Operando studies of $Ce_{0.95}Ni_{0.025}Ru_{0.025}O_2$ during catalysis and reference samples (Ni foil, Ru foil, NiO powder, and RuO_2 powder) using X-ray

absorption spectroscopy (XANES and EXAFS) and corresponding Fourier transformed radical distribution function of Ru K edge and Ni K edge. In these studies, a certain amount of $Ce_{0.95}Ni_{0.025}Ru_{0.025}O_2$ was loaded into the quartz reactor of EXAFS and XANES cells. A mixture of CH_4, CO_2 and He was flowed through the catalyst bed of the EXAFS cell at catalysis temperature. Data collection after sample was cooled to 50–100 °C: (a) energy space of Ru K edge of $Ce_{0.95}Ni_{0.025}Ru_{0.025}O_2$ and Ru foil reference; (b) energy space of Ni K edge of $Ce_{0.95}Ni_{0.025}Ru_{0.025}O_2$ and Ni foil reference. (c) Experimental (black) and fitting (red) r-space spectra of Ru K edge of $Ce_{0.95}Ni_{0.025}Ru_{0.025}O_2$. (d) Experimental (black) and fitting (red) r-space spectra of Ni K edge of $Ce_{0.95}Ni_{0.025}Ru_{0.025}O_2$. (e) r-space spectrum of reference sample Ru foil. (f) r-space spectrum of reference sample Ni foil. (g) r-space spectrum of reference sample RuO_2. (h) r-space spectrum of reference sample NiO. All r-space spectra are shown without phase correction. (i) Coordination environments of Ni_1 and Ru_1 atoms of $Ce_{0.95}Ni_{0.025}Ru_{0.025}O_2$ during catalysis.

From the feature of near-edge absorption of the Ru K edge and Ni K edge collected during catalysis, Ru and Ni atoms of $Ce_{0.95}Ni_{0.025}Ru_{0.025}O_2$ during catalysis are at cationic states (Figures 8a,b). The R-space spectra of the Ni K edge and Ru K edge obtained from EXAFS studies of $Ce_{0.95}Ni_{0.025}Ru_{0.025}O_2$ during catalysis show that Ni and Ru atoms are singly dispersed and coordinated with oxygen atoms during catalysis. The fitting results of the Fourier transformed radical distribution functions (Figure 8c,d) suggest that Ru and Ni are coordinated with O in the first shell and Ce in the second shell during catalysis. As shown in Figure 8i, the fittings of *r*-space of Ni K-edge suggest that (1) each Ni atom bonds with three oxygen atoms on average in the first coordination shell, (2) the distance between Ni and O is 1.90 ± 0.02 Å, (3) each Ni atom coordinates with three Ce atoms in the closest second coordination shell (Ni–O–Ce), and (4) the direct distance between Ni and Ce in Ni–(O)–Ce is 3.10 ± 0.07 Å. Similar fitting of *r*-space of Ru K-edge suggests that (1) each Ru atom bonds with about four oxygen atoms in the first coordination shell, (2) the direct distances between Ru and O are 1.86 ± 0.06 Å and 2.11 ± 0.05 Å, which are close to the 1.90 ± 0.02 Å of Ni–O of this catalyst to some extent, (3) each Ru atom coordinates with three Ce atoms in the closest second coordination shell (Ru–O–Ce), and (4) the direct distance between Ru and Ce is 2.78 ± 0.02 Å, which is a reasonable distance between Ru and Ce since the ionic radii of Ru and Ce are 0.82 and 1.15 Å, respectively,(47) and the ∠Ru–O–Ce is about 55°.
The coordination number and bond distance of Ni_1 and Ru_1 uncovered with operando EXAFS studies (Figure 8i) are consistent with the geometries of Ni_1 and Ru_1 sites on the surface of CeO_2 (110) optimized with DFT calculations (Figure 9). Obviously, the r-space spectra of Ru K-edge and Ni K-edge do not support the existence of the second shell of Ru or Ni atoms in terms of Ru–O–Ru and Ni–O–Ni structure, respectively. Thus, we concluded that Ru and Ni cations are in the format of single dispersion on CeO_2 during catalysis instead of NiO, RuO_2, Ni, or Ru nanoparticles.

Figure 9

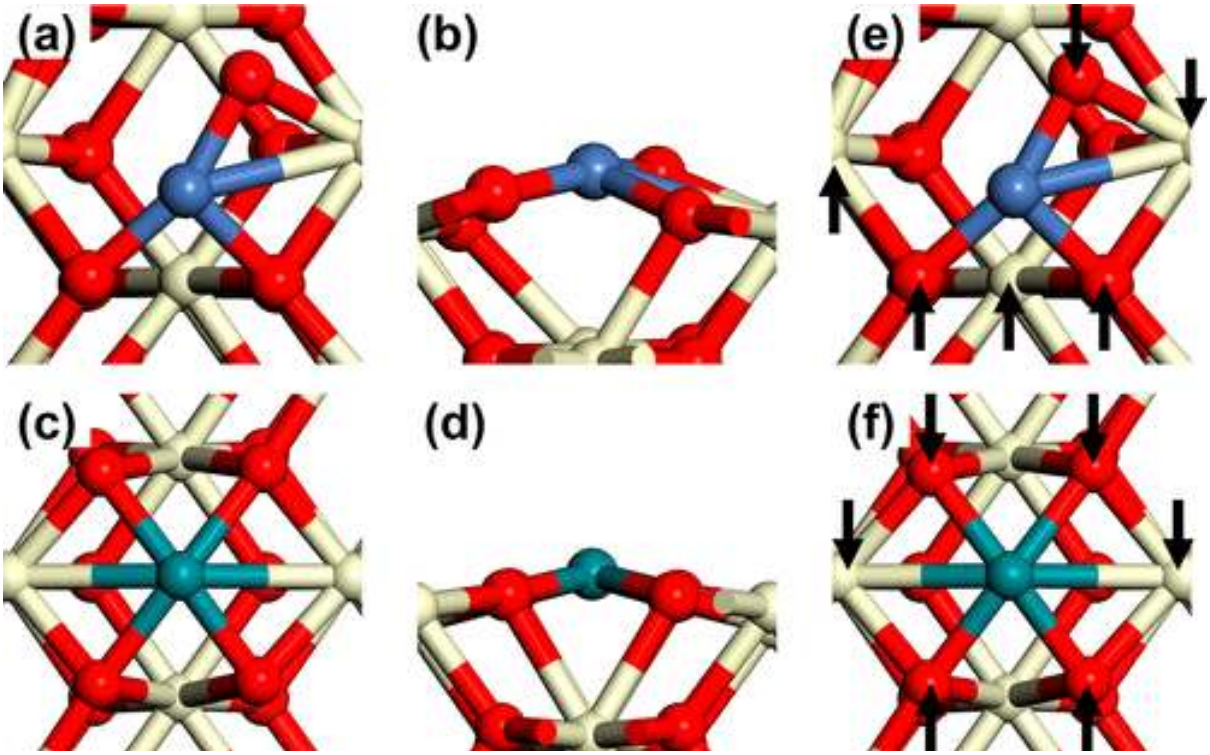

Figure 9. Most stable surface structure representing the surface of $Ru_{0.025}Ni_{0.025}Ce_{0.95}O_2$ during catalysis. (a) Top view of CeO_2 (110) anchored with a Ni_1 atom. (b) Side view of CeO_2 (110) anchored with the Ni_1 atom. (c) Top view of CeO_2 (110) anchored with Ru_1 atoms. (d) Side view of CeO_2 (110) anchored with Ru_1 atoms. (e) Marked neighbor atoms (black arrows) coordinated with Ni_1 site. (f) Marked neighbor atoms (black arrows) coordinated with Ru_1 site. Ce, Ni, and Ru are shown in yellow, blue, and green, respectively. Red balls indicate oxygen atoms. These notations are used throughout this work. It is the most stable surface among four optimized surface structures with different binding environments of Ni_1 and Ru_1 atoms.

4. DFT Calculations

4.1. Different Anchoring Sites of Ni_1 and Ru_1 Atoms

(110) of CeO_2 is the preferentially exposed surface of a $Ru_{0.025}Ni_{0.025}Ce_{0.95}O_2$ on the basis of the above HRTEM studies (Figures S8 and S9). Thus, the (110) surface of CeO_2 nanorods was chosen to build structural models for simulating activation of CH_4 and CO_2 on $Ru_{0.025}Ni_{0.025}Ce_{0.95}O_2$. Four potential doping sites for both Ru_1 and Ni_1 on CeO_2, respectively, were optimized. The most stable doping sites are shown in Figure 9. Chemical and coordination environments of Ni_1 and Ru_1 atoms of the most stable sites offered through optimization with DFT (Figure 9) are listed in Table S1. These bonding parameters (Table S1)

are in good agreement with the coordination environments measured through operando EXAFS studies of Ni K-edge and Ru K-edge (Figure 8i). Therefore, the optimized surface structure in Figure 9 was used for simulating activations of methane and CO_2 molecules to form CO and H_2 in dry reforming of CH_4.

4.2. Activation of the First C–H of CH_4 To Form CH_3 on Ni_1

Activation of methane is one of the most important elementary steps in catalytic transformation of CH_4 according to previous work.(20,48−50) On the basis of the optimized structure (Figure 9), here dissociative chemisorptions of methane on Ru_1 and Ni_1 sites were investigated. Geometries of the most favorable transition states in activation of the first C–H of methane on Ni_1 and Ru_1 atoms are shown in Figure 10a,b (for Ni_1) and Figure 10c,d (for Ru_1), respectively. On the basis of these DFT calculations, Gibbs free energy barriers for activations of the first C–H of CH_4 on Ni_1 and Ru_1 sites are 1.88 and 2.01 eV, respectively. These values suggest that Ni_1 is the preferred active site for activating the first C–H of methane since the barrier on Ni_1 is relatively lower in contrast to Ru_1. In fact, the activation barrier of C–H of methane on the Ni_1, 1.88 eV, is low in contrast to the activation barriers of the first C–H of methane on other catalysts,(15) which is consistent with the quite high activity of dry reforming at a relatively low temperature observed in this work. The formed CH_3 and H adsorb on a Ni atom and an O atom of the surface lattice, respectively (Figure 10e,f).

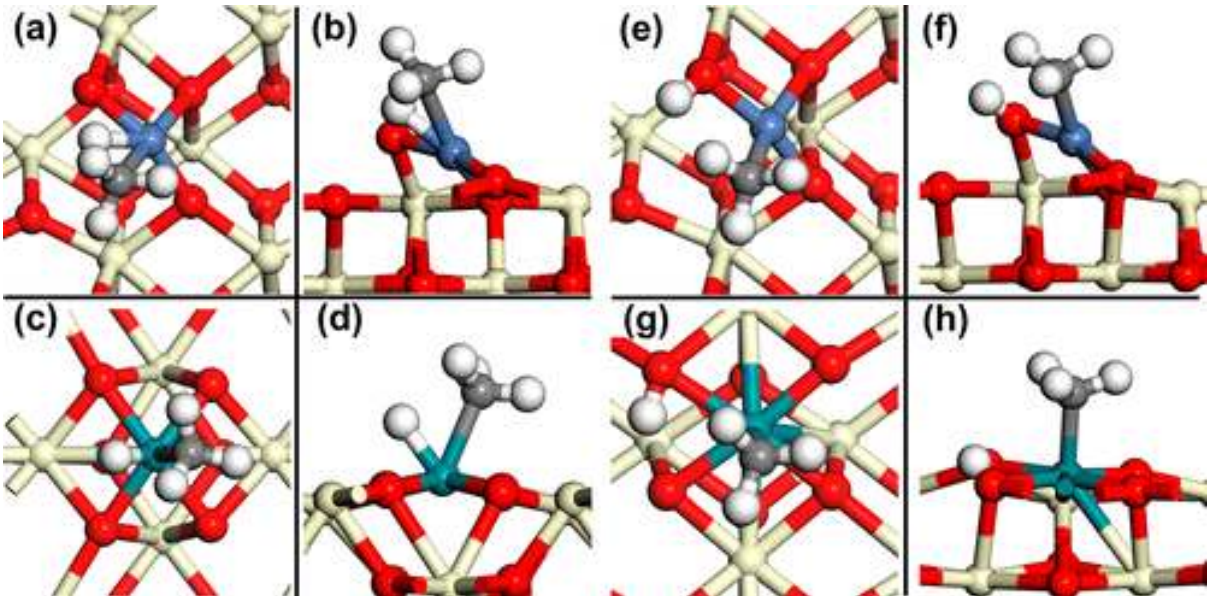

Figure 10. Top views and side views of transition-state geometries of CH_4 activation and intermediate structures of formed CH_3 and H on Ni_1 and Ru_1 sites on CeO_2. Top and side views of transition-state geometries of CH_4 activation on Ni_1 ((a and b) and Ru_1 (c and d), intermediate geometries of CH_3 and H formed on Ni_1 site (e and f) and Ru_1 site (g and h).

4.3. Transformation of CH_3 to CO and H on Ni_1

Transformation of CH_4 to CO can be done through four dehydrogenation steps to form H atoms and C atom; the formed C atom is then oxidized to form CO. Due to the high mobility of surface lattice oxygen atoms, the possibility of coupling between oxygen atom of surface lattice and carbon atom formed through activation of methane is considered here.

After the formation of CH_3 species, two different types of reactions including (1) dehydrogenation of CH_3 into CH_2 and H and (2) oxidation of CH_3 to CH_3O are considered here for transforming CH_3 to CO. Both of them were investigated. The transition-state geometries of these two potential steps on a Ni_1 site and a Ru_1 site are shown in Figure S8a–d and Figure S8e–h, respectively. The calculated activation energies of CH_3 dehydrogenation performed on a Ni_1 site (Figure S8a,b) and CH_3 oxidation on a Ni_1 site (Figure S8c,d) are 1.39 and 1.33 eV, respectively. Therefore, the dehydrogenation of CH_3 on a Ni_1 site to form CH_2 and H and oxidation of CH_3 on a Ni_1 site to CH_3O are kinetically similar. However, the free energy changes for dehydrogenation of CH_3 on a Ni_1 site and oxidation of CH_3 to CH_3O on a Ni_1 site are +0.50 and −0.03 eV, respectively. Thus, in terms of Ni_1 site, the oxidation of CH_3 to CH_3O is likely to be the dominant pathway in contrast to the dehydrogenation of CH_3 into CH_2 and H on Ni_1 site.

Parallel to the above investigations on a Ni_1 site, dehydrogenation of CH_3 to CH_2 or oxidation of CH_3 on a Ru_1 site were studied as well. The activation barrier for dehydrogenation of CH_3 to CH_2 and H on a Ru_1 site and oxidation of CH_3 to CH_3O on a Ru_1 site are 1.73 and 2.22 eV, respectively. The free energy change for the dehydrogenation and oxidation on a Ru_1 site is 0.69 and 0.58 eV, respectively. Thus, obviously both dehydrogenation of CH_3 to CH_2 and H and oxidation of CH_3 to CH_3O on a Ni_1 site are kinetically favorable in contrast to a Ru_1 site. For instance, compared to the dehydrogenation of CH_3 to CH_2 on a Ru_1 with an activation barrier of 1.73 eV and free energy change of 0.69 eV, the oxidation of CH_3 to CH_3O on a Ni_1 site (with activation barrier of 1.33 eV and free energy change of −0.03 eV) is thermodynamically favorable. Thus, upon the activation of the first C–H of CH_4, a favorable step is oxidation of CH_3 to CH_3O on a Ni_1 site.

With similar methods, all possible steps of dehydrogenation of CH_2 and CH and oxidation of CH_2 to CH_2O, CH to CHO, and C to CO on Ni_1 and Ru_1 sites were systematically investigated. The favorable pathways from activation of the first C–H of CH_4 to formation of CO on Ni_1 sites are listed in Table S2. For comparison, Table S2 lists the pathways from activation of CH_4 to the formation of CO on the Ru_1 site as well.

As shown in Table S2, most of the dehydrogenation steps after the third step are favorable with low free energy barriers and negative Gibbs free energy changes on a Ru_1 site. In addition, the steps of desorption of CO from the Ni_1 site and the Ru_1 site are endothermic and barrierless (step 6 in Table S2). Notably, the bonding of CO on a Ru_1 site is much stronger than on a Ni_1 site, which likely results in a high coverage of CO on Ru_1 sites and therefore limits

the reaction rate. In general, the activation energies of elementary steps on a Ni_1 site are lower than those on a Ru_1 site as shown in Table S2, indicating that a Ni_1 site is more active in the transformation of CH_3 to CO. Overall, DFT calculations suggest that a Ni_1 site is responsible for the activation of CH_4 to form CO. In the potential pathway presented in Table S2, the highest free energy barrier among these elementary steps is the activation of the first C–H bond of CH_4 on both Ni_1 and Ru_1 sites. It suggests that methane activation is the rate-determining step of reforming CH_4 with CO_2 on $Ce_{0.95}Ni_{0.025}Ru_{0.025}O_2$.

4.4. Activation of CO_2 To Form CO and O on $Ru_1 + O_{vac}$

Due to the formation of a CO molecule from CH_4 on a catalyst surface, a lattice oxygen atom is consumed from the surface of CeO_2 and thus an oxygen vacancy is created. The oxygen vacancy needs to be filled so that the surface lattice oxygen atoms can continuously function in oxidation steps of the next catalytic cycle. For instance, the transition state of the step from CH_4 to CH_3 is a four-membered ringlike structure involving the bindings of C and H atoms of CH_4 to Ni and surface lattice O atom, respectively (Figure 10a,b). In dry reforming ($CH_4 + CO_2 = 2CO + 2H_2$), carbon dioxide is the only source to provide oxygen atoms to fill oxygen vacancies of the catalyst surface. Here, activations of CO_2 on Ni_1 and Ru_1 sites together with refilling of oxygen vacancies were investigated. It is found that the Gibbs free energy barriers (G_a) of dissociating CO_2 on a Ni_1 and a Ru_1 site are 1.23 and 0.01 eV, respectively. Thus, activation of CO_2 on $Ru_1 + O_{vac}$ is much more kinetically favorable than $Ni_1 + O_{vac}$. After crossing this transition state (Figure S9a,b), the formed CO binds to Ni_1 and the formed O fills O_{vac} next to Ni_1. The formed CO and O atom are adsorbed on Ru_1 fill to O_{vac} next to Ru_1 (Figure S9g,h). As shown in Figure S9a,b, the activation of CO_2 on Ni_1 and Ru_1 involves oxygen vacancies next to Ni_1 and Ru_1 atoms, respectively. Gibbs free energy changes in dissociation of CO_2 on $Ni_1 + O_{vac}$ and $Ru_1 + O_{vac}$ to form the adsorbed CO and O are 0.76 and −0.99 eV, respectively, suggesting that $Ru_1 + O_{vc}$ is a thermodynamically favorable site. Thus, $Ru_1 + O_{vac}$ is kinetically and thermodynamically favorable for activation of CO_2 in contrast to $Ni_1 + O_{vac}$. The activation of CO_2 on $Ru_1 + O_{vac}$ forms the second CO molecule of the reforming ($CH_4 + CO_2 = 2CO + 2H_2$).

4.5. Coupling of H Atoms To Form H_2 on Ru_1

Other than formation of CO through activation of CH_4 to CH_n (n = 0–3) along with progressive oxidation of CH_n (n = 0–3) to CO, H atoms are formed in the pathway of transferring CH_4 to CO as shown in Table S2. Coupling of these formed H atoms on surface to form H_2 is a necessary step. This step was simulated. Transition states for coupling hydrogen atoms on Ni_1 and Ru_1 sites are shown in Figure S10. The calculated activation barriers for coupling H atoms on Ni_1 and Ru_1 are 1.96 and 0.65 eV, respectively, while the free energies changes for coupling hydrogen atoms to form a H_2 molecule on Ni_1 and Ru_1 sites are 0.63 and 0.26 eV, respectively. Therefore, the Ru_1 site

should be responsible for coupling atomic hydrogen to form H_2 molecules since coupling of H atoms on Ru_1 is thermodynamically and kinetically favorable.

4.6. Synergy Effect of Ni_1 and Ru_1 in Reforming CH_4 with CO_2

The chemical and coordination environments of Ni atoms and Ru atoms of optimized $CeO_2(110)$ with anchored Ni_1 and Ru_1 atoms proposed through DFT calculations are consistent with the catalyst structure of experimental characterization using in situ/operando approaches, suggesting that the structural model optimized with these DFT calculations is suitable for exploring mechanism of reforming of CH_4 with CO_2. The activations of CH_4 and CO_2 and coupling of H atoms were simulated with all the possible elementary steps on Ni_1, Ru_1, Ni_1 + Vac, and Ru_1 + Vac. It is found that Ni_1 and its adjacent oxygen atom are highly active for the activation of methane to form both CO and oxygen vacancy with a low activation barrier, offering high activity of reforming methane on $Ce_{0.95}Ni_{0.025}Ru_{0.025}O_2$ at a relatively low temperature. Ru_1 + O_{vac} is responsible for activating another reactant. The different roles of a Ni_1 site (for activation of CH_4) and a Ru_1 site (for activation of CO_2) of $Ce_{0.95}Ni_{0.025}Ru_{0.025}O_2$ clearly justified the synergistic effect between Ni_1 and Ru_1 observed experimentally.
As shown in sections 4.2, 4.3, and 4.5, the formed H atoms in the steps of activating CH_4 to form CO on a Ni_1 site prefer to couple each other to form a H_2 molecule on a Ru_1 site. Thus, the first formation of H atoms on a Ni_1 site and then coupling H atoms to form H_2 molecules on a Ru_1 site is another synergistic effect between Ni_1 and Ru_1 sites of $Ce_{0.95}$ $Ni_{0.025}Ru_{0.025}O_2$; in other words, Ni_1 and Ru_1 sites play a *sequential* role in *first* generation of H atoms on Ni_1 sites and *then* coupling H atoms to form H_2 on a Ru_1 site in a catalytic cycle. Thus, these DFT calculations provided molecular pictures of the two synergy effects of the two sets of single-atom sites (Ni_1 and Ru_1) on $Ce_{0.95}$ $Ni_{0.025}Ru_{0.025}O_2$.

5. Summary

Two sets of single-atom sites, Ni_1 and Ru_1, were successfully anchored on the surface of CeO_2 nanorods, forming a catalyst of dual single-atom sites, $Ce_{0.95}Ni_{0.025}Ru_{0.025}O_2$. It is highly active for reforming methane with CO_2 to produce syngas (CO + H_2) with a selectivity of 98.5% for producing H_2 with an unprecedented high activity in terms of TOF of 73.6 H_2 per site per second at 560 °C. The synergistic effect between Ru_1 an Ni_1 on $Ce_{0.95}Ni_{0.025}Ru_{0.025}O_2$ were confirmed by its lowest apparent activation barrier and highest turnover rate of forming CO and H_2 among $Ce_{0.95}Ni_{0.025}Ru_{0.025}O_2$, $Ce_{0.95}Ru_{0.05}O_2$ and $Ce_{0.95}Ni_{0.05}O_2$. Computational studies uncovered that the molecular-level origins of synergistic effects of Ni_1 and Ru_1 sites are (1) the complementary function of Ni_1 (for activation of CH_4) and of Ru_1 (for activation of CO_2) and (2) the

sequential role of *first* generating H atoms in activating CH_4 on a Ni_1 site and *then* coupling H atoms to form H_2 on a Ru_1 site. These reported synergistic effects demonstrated a new avenue for designing a catalyst with high activation and selectivity at a low temperature.

Supporting Information

The Supporting Information is available free of charge on the ACS Publications website at DOI: 10.1021/jacs.8b10910.

Characterization data, influence of gas-phase molecules, measurement of catalytic performance, stability of catalytic activity, and DFT calculations (PDF)

References

1. Schwach, P.; Pan, X.; Bao, X. Direct Conversion of Methane to Value-Added Chemicals over Heterogeneous Catalysts: Challenges and Prospects. *Chem. Rev.* **2017**, *117* (13), 8497– 8520, DOI: 10.1021/acs.chemrev.6b00715

2. Spivey, J. J.; Hutchings, G. Catalytic aromatization of methane. *Chem. Soc. Rev.* **2014**, *43* (3), 792– 803, DOI: 10.1039/C3CS60259A

3. Guo, X.; Fang, G.; Li, G.; Ma, H.; Fan, H.; Yu, L.; Ma, C.; Wu, X.; Deng, D.; Wei, M. Direct, nonoxidative conversion of methane to ethylene, aromatics, and hydrogen. *Science* **2014**, *344* (6184), 616– 619, DOI: 10.1126/science. 1253150

4. Yi, N.; Cao, Y.; Liu, Y.-M.; Dai, W.-L.; He, H.-Y.; Fan, K.-N. Highly Efficient Ni–Ce–O Mixed Oxide Catalysts via Gel-coprecipitation of Oxalate Precursors for Catalytic Combustion of Methane. *Chem. Lett.* **2005**, *34* (1), 108– 109, DOI: 10.1246/cl.2005.108

5. Lunsford, J. H. Catalytic conversion of methane to more useful chemicals and fuels: a challenge for the 21st century. *Catal. Today* **2000**, *63* (2–4), 165– 174, DOI: 10.1016/S0920-5861(00)00456-9

6. Pena, M. A.; Gomez, J. P.; Fierro, J. L. G. New catalytic routes for syngas and hydrogen production. *Appl. Catal., A* **1996**, *144* (1–2), 7– 57, DOI: 10.1016/0926-860X(96)00108-1

7. Song, C. S.; Pan, W. Tri-reforming of methane: a novel concept for catalytic production of industrially useful synthesis gas with desired H-2/CO

ratios. *Catal. Today* **2004**, *98* (4), 463– 484, DOI: 10.1016/j.cattod.2004.09.054

8. Pakhare, D.; Spivey, J. A review of dry (CO 2) reforming of methane over noble metal catalysts. *Chem. Soc. Rev.* **2014**, *43* (22), 7813– 7837, DOI: 10.1039/C3CS60395D

9. Gonzalez-delaCruz, V. M.; Pereñiguez, R.; Ternero, F.; Holgado, J. P.; Caballero, A. In situ XAS study of synergic effects on Ni–Co/ZrO2 methane reforming catalysts. *J. Phys. Chem. C* **2012**, *116* (4), 2919– 2926, DOI: 10.1021/jp2092048

10. Fan, M. S.; Abdullah, A. Z.; Bhatia, S. Catalytic technology for carbon dioxide reforming of methane to synthesis gas. *ChemCatChem* **2009**, *1* (2), 192– 208, DOI: 10.1002/cctc.200900025

11. Hansen, T. W.; DeLaRiva, A. T.; Challa, S. R.; Datye, A. K. Sintering of catalytic nanoparticles: particle migration or Ostwald ripening?. *Acc. Chem. Res.* **2013**, *46* (8), 1720– 1730, DOI: 10.1021/ar3002427

12. Trimm, D. L. Coke formation and minimisation during steam reforming reactions. *Catal. Today* **1997**, *37* (3), 233– 238, DOI: 10.1016/S0920-5861(97)00014-X

13. Trimm, D. L. Catalysts for the control of coking during steam reforming. *Catal. Today* **1999**, *49* (1–3), 3– 10, DOI: 10.1016/S0920-5861(98)00401-5

14. Ginsburg, J. M.; Piña, J.; El Solh, T.; De Lasa, H. I. Coke formation over a nickel catalyst under methane dry reforming conditions: thermodynamic and kinetic models. *Ind. Eng. Chem. Res.* **2005**, *44* (14), 4846– 4854, DOI: 10.1021/ie0496333

15. Wang, Z.; Cao, X.-M.; Zhu, J.; Hu, P. Activity and coke formation of nickel and nickel carbide in dry reforming: a deactivation scheme from density functional theory. *J. Catal.* **2014**, *311*, 469– 480, DOI: 10.1016/j.jcat.2013.12.015

16. Lustemberg, P. G.; Ramírez, P. J.; Liu, Z.; Gutiérrez, R. A.; Grinter, D. G.; Carrasco, J.; Senanayake, S. D.; Rodriguez, J. A.; Ganduglia-Pirovano, M. V. Room-Temperature Activation of Methane and Dry Re-forming with CO2 on Ni-CeO2(111) Surfaces: Effect of Ce3+ Sites and Metal–Support Interactions on C–H Bond Cleavage. *ACS Catal.* **2016**, *6* (12), 8184– 8191, DOI: 10.1021/acscatal.6b02360

17. Rodriguez, J. A.; Grinter, D. C.; Liu, Z.; Palomino, R. M.; Senanayake, S. D. Ceria-based model catalysts: fundamental studies on the importance of the metal–ceria interface in CO oxidation, the water–gas shift, CO 2 hydrogenation, and methane and alcohol reforming. *Chem. Soc. Rev.* **2017**, *46* (7), 1824– 1841, DOI: 10.1039/C6CS00863A

18. Xu, W.; Liu, Z.; Johnston-Peck, A. C.; Senanayake, S. D.; Zhou, G.; Stacchiola, D.; Stach, E. A.; Rodriguez, J. A. Steam reforming of ethanol on Ni/CeO2: reaction pathway and interaction between Ni and the CeO2 support. *ACS Catal.* **2013**, *3* (5), 975– 984, DOI: 10.1021/cs4000969

19. Zhang, S.; Nguyen, L.; Liang, J.-X.; Shan, J.; Liu, J.; Frenkel, A. I.; Patlolla, A.; Huang, W.; Li, J.; Tao, F. Catalysis on singly dispersed bimetallic sites. *Nat. Commun.* **2015**, *6*, 7938, DOI: 10.1038/ncomms8938

20. Tao, F. F.; Shan, J.-j.; Nguyen, L.; Wang, Z.; Zhang, S.; Zhang, L.; Wu, Z.; Huang, W.; Zeng, S.; Hu, P. Understanding complete oxidation of methane on spinel oxides at a molecular level. *Nat. Commun.* **2015**, *6*, 7798, DOI: 10.1038/ncomms8798

21. Zhang, S.; Tang, Y.; Nguyen, L.; Zhao, Y.-F.; Wu, Z.; Goh, T.-W.; Liu, J. J.; Li, Y.; Zhu, T.; Huang, W. Catalysis on Singly Dispersed Rh Atoms Anchored on an Inert Support. *ACS Catal.* **2018**, *8* (1), 110– 121, DOI: 10.1021/acscatal.7b01788

22. Nguyen, L.; Zhang, S.; Wang, L.; Li, Y.; Yoshida, H.; Patlolla, A.; Takeda, S.; Frenkel, A. I.; Tao, F. Reduction of Nitric Oxide with Hydrogen on Catalysts of Singly Dispersed Bimetallic Sites Pt1Co m and Pd1Co n. *ACS Catal.* **2016**, *6* (2), 840– 850, DOI: 10.1021/acscatal.5b00842

23. Fung, V.; Tao, F.; Jiang, D. E. Low-temperature activation of methane on doped single atoms: descriptor and prediction. *Phys. Chem. Chem. Phys.* **2018**, *20* (35), 22909– 22914, DOI: 10.1039/C8CP03191F

24. Shan, J.; Huang, W.; Nguyen, L.; Yu, Y.; Zhang, S.; Li, Y.; Frenkel, A. I.; Tao, F. Conversion of methane to methanol with a bent mono (μ-oxo) dinickel anchored on the internal surfaces of micropores. *Langmuir* **2014**, *30* (28), 8558– 8569, DOI: 10.1021/la501184b

25. Liu, Z.; Grinter, D. C.; Lustemberg, P. G.; Nguyen-Phan, T. D.; Zhou, Y.; Luo, S.; Waluyo, I.; Crumlin, E. J.; Stacchiola, D. J.; Zhou, J. Dry Reforming of Methane on a Highly-Active Ni-CeO2 Catalyst: Effects of Metal-Support Interactions on C– H Bond Breaking. *Angew. Chem., Int. Ed.* **2016**, *55* (26), 7455– 7459, DOI: 10.1002/anie.201602489

26. Yan, B.; Yang, X.; Yao, S.; Wan, J.; Myint, M.; Gomez, E.; Xie, Z.; Kattel, S.; Xu, W.; Chen, J. G. Dry reforming of ethane and butane with CO2 over PtNi/CeO2 bimetallic catalysts. *ACS Catal.* **2016**, *6* (11), 7283– 7292, DOI: 10.1021/acscatal.6b02176

27. Zhu, Y.; Zhang, S.; Shan, J.-j.; Nguyen, L.; Zhan, S.; Gu, X.; Tao, F. In situ surface chemistries and catalytic performances of ceria doped with palladium, platinum, and rhodium in methane partial oxidation for the production of syngas. *ACS Catal.* **2013**, *3* (11), 2627– 2639, DOI: 10.1021/cs400070y

28. Xie, Z. H.; Yan, B. H.; Kattel, S.; Lee, J. H.; Yao, S. Y.; Wu, Q. Y.; Rui, N.; Gomez, E.; Liu, Z. Y.; Xu, W. Q.; Zhang, L.; Chen, J. G. G. Dry reforming of methane over CeO2-supported Pt-Co catalysts with enhanced activity. *Appl. Catal., B* **2018**, *236*, 280– 293, DOI: 10.1016/j.apcatb.2018.05.035

29. Mai, H.-X.; Sun, L.-D.; Zhang, Y.-W.; Si, R.; Feng, W.; Zhang, H.-P.; Liu, H.-C.; Yan, C.-H. Shape-selective synthesis and oxygen storage behavior of ceria nanopolyhedra, nanorods, and nanocubes. *J. Phys. Chem. B* **2005**, *109* (51), 24380– 24385, DOI: 10.1021/jp055584b

30. Jones, J.; Xiong, H.; DeLaRiva, A. T.; Peterson, E. J.; Pham, H.; Challa, S. R.; Qi, G.; Oh, S.; Wiebenga, M. H.; Hernández, X. I. P. Thermally stable single-atom platinum-on-ceria catalysts via atom trapping. *Science* **2016**, *353* (6295), 150– 154, DOI: 10.1126/science.aaf8800

31. Wu, Z.; Schwartz, V.; Li, M.; Rondinone, A. J.; Overbury, S. H. Support shape effect in metal oxide catalysis: ceria-nanoshape-supported vanadia catalysts for oxidative dehydrogenation of isobutane. *J. Phys. Chem. Lett.* **2012**, *3* (11), 1517– 1522, DOI: 10.1021/jz300513u

32. Kresse, G.; Furthmüller, J. Efficient iterative schemes for ab initio total-energy calculations using a plane-wave basis set. *Phys. Rev. B: Condens. Matter Mater. Phys.* **1996**, *54* (16), 11169– 11186, DOI: 10.1103/PhysRevB.54.11169

33. Kresse, G.; Furthmuller, J. Efficiency of ab-initio total energy calculations for metals and semiconductors using a plane-wave basis set. *Comput. Mater. Sci.* **1996**, *6* (1), 15– 50, DOI: 10.1016/0927-0256(96)00008-0

34. Kresse, G.; Hafner, J. Ab-Initio Molecular-Dynamics Simulation of the Liquid-Metal Amorphous-Semiconductor Transition in Germanium. *Phys. Rev. B: Condens. Matter Mater. Phys.* **1994**, *49* (20), 14251– 14269, DOI: 10.1103/PhysRevB.49.14251

35. Kresse, G.; Hafner, J. Ab initio molecular dynamics for liquid metals. *Phys. Rev. B: Condens. Matter Mater. Phys.* **1993**, *47* (1), 558– 561, DOI: 10.1103/PhysRevB.47.558

36. Perdew, J. P.; Burke, K.; Ernzerhof, M. Generalized Gradient Approximation Made Simple. *Phys. Rev. Lett.* **1996**, *77* (18), 3865– 3868, DOI: 10.1103/PhysRevLett.77.3865

37. Kresse, G.; Joubert, D. From ultrasoft pseudopotentials to the projector augmented-wave method. *Phys. Rev. B: Condens. Matter Mater. Phys.* **1999**, *59* (3), 1758– 1775, DOI: 10.1103/PhysRevB.59.1758

38. Blöchl, P. E. Projector augmented-wave method. *Phys. Rev. B: Condens. Matter Mater. Phys.* **1994**, *50* (24), 17953– 17979, DOI: 10.1103/PhysRevB.50.17953

39. Mullins, D.; Overbury, S.; Huntley, D. Electron spectroscopy of single crystal and polycrystalline cerium oxide surfaces. *Surf. Sci.* **1998**, *409* (2), 307– 319, DOI: 10.1016/S0039-6028(98)00257-X

40. Paparazzo, E. On the curve-fitting of XPS Ce (3d) spectra of cerium oxides. *Mater. Res. Bull.* **2011**, *46* (2), 323– 326, DOI: 10.1016/j.materresbull.2010.11.009

41. Newberg, J. T.; Starr, D. E.; Yamamoto, S.; Kaya, S.; Kendelewicz, T.; Mysak, E. R.; Porsgaard, S.; Salmeron, M. B.; Brown, G. E.; Nilsson, A. Formation of hydroxyl and water layers on MgO films studied with ambient pressure XPS. *Surf. Sci.* **2011**, *605* (1), 89– 94, DOI: 10.1016/j.susc.2010.10.004

42. Morgan, D. J. Resolving ruthenium: XPS studies of common ruthenium materials. *Surf. Interface Anal.* **2015**, *47* (11), 1072– 1079, DOI: 10.1002/sia.5852

43. Chastain, J.; King, R. C.; Moulder, J. *Handbook of X-ray photoelectron spectroscopy: a reference book of standard spectra for identification and interpretation of XPS data*; Physical Electronics Division, Perkin-Elmer Corp., Eden Prairie, MN, **1992.**

44. Grosvenor, A. P.; Biesinger, M. C.; Smart, R. S. C.; McIntyre, N. S. New interpretations of XPS spectra of nickel metal and oxides. *Surf. Sci.* **2006**, *600* (9), 1771– 1779, DOI: 10.1016/j.susc.2006.01.041

45. Sangaletti, L.; Depero, L.; Parmigiani, F. On the non-local screening mechanisms in the 2p photoelectron spectra of NiO and La2NiO4. *Solid State Commun.* **1997**, *103* (7), 421– 424, DOI: 10.1016/S0038-1098(97)00185-3

46. Ravel, B.; Newville, M. ATHENA, ARTEMIS, HEPHAESTUS: data analysis for X-ray absorption spectroscopy using IFEFFIT. *J. Synchrotron Radiat.* **2005**, *12* (4), 537– 541, DOI: 10.1107/S0909049505012719

47. Shannon, R. D. *Acta Crystallogr., Sect. A: Cryst. Phys., Diffr., Theor. Gen. Crystallogr.* **1976**, *32*, 751, DOI: 10.1107/S0567739476001551

48. Wang, Z.; Cao, X. M.; Zhu, J.; Hu, P. Activity and coke formation of nickel and nickel carbide in dry reforming: A deactivation scheme from density functional theory. *J. Catal.* **2014**, *311* (0), 469– 480, DOI: 10.1016/j.jcat.2013.12.015

49. Jones, G.; Jakobsen, J. G.; Shim, S. S.; Kleis, J.; Andersson, M. P.; Rossmeisl, J.; Abild-Pedersen, F.; Bligaard, T.; Helveg, S.; Hinnemann, B.; Rostrup-Nielsen, J. R.; Chorkendorff, I.; Sehested, J.; Norskov, J. K. First principles calculations and experimental insight into methane steam reforming over transition metal catalysts. *J. Catal.* **2008**, *259* (1), 147– 160, DOI: 10.1016/j.jcat.2008.08.003

50. Tang, Y.; Li, Y.; Fung, V.; Jiang, D.-e.; Huang, W.; Zhang, S.; Iwasawa, Y.; Sakata, T.; Nguyen, L.; Zhang, X. Single rhodium atoms anchored in micropores for efficient transformation of methane under mild conditions. *Nat. Commun.* **2018**, *9* (1), 1231, DOI: 10.1038/s41467-018-03235-7